

Article

Role of Microalloying Elements on Recrystallization Kinetics of Cold-Rolled High Strength Low Alloy Steels

Shuai Tang , Xiaofang Li, Jianping Li, Zhenyu Liu and Guodong Wang

State Key Laboratory of Rolling and Automation, Northeastern University, Shenyang 110819, China

* Correspondence: tangshuai@ral.neu.edu.cn; Tel.: +86-24-83686419

Abstract: The recrystallization kinetics of two cold-rolled high strength low alloy steels with the addition of Ti and Ti-V, respectively, during annealing were investigated by means of modeling and experimental validation. The recrystallization kinetics of the Ti-V steel were hindered compared to the Ti steel. Based on solid solution theory, mass conservation law and classical nucleation, growth and coarsening theory, the precipitation behavior of Ti and Ti-V steels was predicted. The radius of TiC is larger, and its number density is lower than $(Ti_x, V_{1-x})C$. On this basis, by considering the comprehensive effect of recrystallization on stored energy, the effect of the microalloyed precipitates and microalloying solute on the driving force and grain boundary mobility, the model of the recrystallization kinetics was proposed, which could well reproduce the effect of microalloying elements on recrystallization. Moreover, it was indicated that solute drag is more effective in retarding recrystallization than the pinning effect of precipitates.

Keywords: recrystallization kinetics; model; microalloying elements; precipitation



Citation: Tang, S.; Li, X.; Li, J.; Liu, Z.; Wang, G. Role of Microalloying Elements on Recrystallization Kinetics of Cold-Rolled High Strength Low Alloy Steels. *Metals* **2022**, *12*, 1741. <https://doi.org/10.3390/met12101741>

Academic Editor: Elena Pereloma

Received: 31 August 2022

Accepted: 12 October 2022

Published: 17 October 2022

Publisher's Note: MDPI stays neutral with regard to jurisdictional claims in published maps and institutional affiliations.



Copyright: © 2022 by the authors. Licensee MDPI, Basel, Switzerland. This article is an open access article distributed under the terms and conditions of the Creative Commons Attribution (CC BY) license (<https://creativecommons.org/licenses/by/4.0/>).

1. Introduction

Steel materials account for 65% to 70% of vehicle weight. The light weight of automobile steel is of great significance for energy saving and emission reduction. High strength, low alloy (HSLA) steel has the advantages of low cost, easy formation and good welding performance, which is why it is widely used in automotive reinforcements and structural parts [1,2].

HSLA steel is usually designed by adding a small number of microalloying elements on the basis of plain steel. The main strengthening mechanisms in HSLA steels are grain refinement and precipitation hardening. Niobium (Nb), titanium (Ti) and vanadium (V) are added individually or in a combined form with a certain proportion [3–5], forming nano-scaled precipitates, which supply precipitation hardening and retards recrystallization, leading to refined grain size.

During the annealing of cold-rolled HSLA steel, two metallurgical phenomena occur, i.e., ferrite recrystallization and microalloyed precipitation, in which the proceeding of recrystallization may be affected by both solute drag [6–8] and precipitates [9,10] of the microalloyed elements. From a practical point of view, a complete recrystallized microstructure is preferred in order to achieve microstructural uniformity to ensure high performance in mechanical properties and high formability.

At present, high strength cold-rolled HSLA steel is commonly produced in continuous annealing lines, in which the cold-rolled sheets are annealed with a relatively high heating rate and short soaking time [11–13]. In this scenario, it is tough to ensure complete ferrite recrystallization as well as abundant and fine-sized precipitates.

In this study, the recrystallization kinetics, precipitation behavior and texture evolution of two HSLA steels with microalloying elements of Ti and Ti+V were investigated. The recrystallization kinetics were modeled and experimentally validated considering the retardation effect of solute drag and the pinning effect of microalloyed precipitates. Additionally, the texture evolution and its effect on recrystallization were comparatively analyzed.

2. Materials and Methods

The steels were prepared as 50 kg ingots in a vacuum induction furnace. The chemical composition was measured by inductively coupled plasma mass spectrometry (ICP-MS). The main chemical composition is listed in Table 1. Furthermore, the nitrogen content was tested to be 0.0012 wt% for both steels. The ingots were forged into blocks with a thickness of 50 mm. The blocks were heated to 1250 °C and soaked for 2 h, and then they were hot-rolled with 7 passes to the thickness of 4 mm with the finish rolling temperature 900 °C by a Φ 450 reversible hot rolling mill. In order to limit the precipitation in austenite, the 5th pass was carried out above 950 °C. After hot rolling, the steel plates were cooled to 550 °C with a cooling rate of 100 °C/s, then slowly cooled to room temperature. Fast cooling could avoid the precipitation in ferrite at the utmost. In order to facilitate the comparison of different processes, the two steels containing Ti and Ti+V were marked as the Ti sample and Ti-V sample, respectively.

Table 1. Main chemical composition of experimental steel (wt%).

Samples	C	Si	Mn	Ti	V
Ti steel	0.071	0.20	1.20	0.050	-
Ti-V steel	0.070	0.20	1.21	0.051	0.040

The hot-rolled plates were subsequently cold-rolled to a 1.0 mm thickness with a total rolling reduction of 75%. The cold-rolled sheets were machined into samples with a size of 12 × 60 mm², and annealing experiments were performed on an MMS-300 thermal simulator. Samples were heated to 660 °C, 690 °C and 720 °C at a heating rate of 5 °C/s and soaked for 0 to 6000 s and then quenched to room temperature at a cooling rate of 40 °C/s.

Samples were cut, metallographically prepared and etched with a 4% nital solution and observed using a BX53MRF Olympus optical microscope (OM) and a Zeiss Ultra 55 field emission gun scanning electron microscope (FEG-SEM). Specimens for electron backscattered diffraction (EBSD) analysis were mechanically polished and electro-polished with a solution of 90 vol% alcohol and 10 vol% perchloric acid. The EBSD studies were carried out in FEG-SEM (Zeiss Ultra 55) for automatic orientation mapping with a 0.3 μ m step size. EBSD data was processed using HKL CHANNEL 5 software. Microhardness values were measured using an FM-700 microhardness tester with an applied load of 300 g and a dwell time of 10 s.

The recrystallization fraction of ferrite with different annealing temperatures and isothermal times can be calculated from the softening rate formula [14] as follows:

$$X(t) = \frac{HV_0 - HV_t}{HV_0 - HV_{\text{rex}}}, \quad (1)$$

where HV_{rex} is the microhardness of completely recrystallized ferrite, HV_0 is the microhardness before annealing and HV_t is the microhardness under different isothermal time.

3. Results and Discussion

3.1. Initial Microstructure

The microstructures of the hot-rolled Ti and Ti-V steels are shown in Figure 1. One can see that the microstructure in Ti steel is composed of ferrite and a small portion of bainite (Figure 1a). Additionally, the microstructure of Ti-V steel is mainly bainite with remarkably refined morphology (Figure 1b).

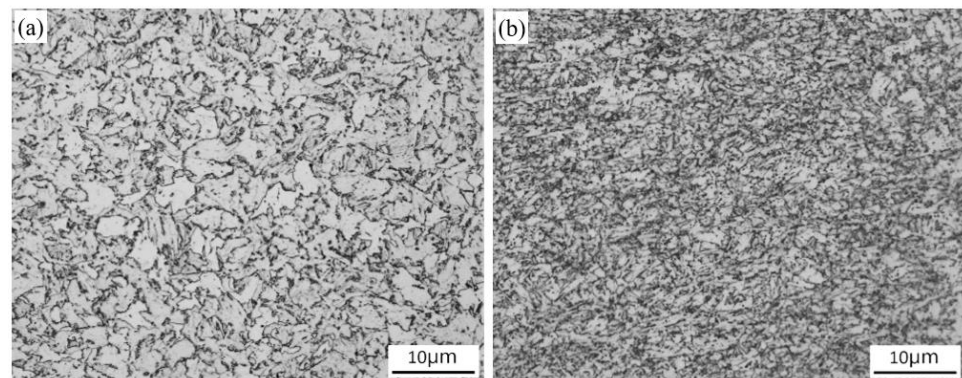


Figure 1. Microstructure of different specimens after hot rolling: (a) Ti steel and (b) Ti-V steel.

3.2. Recrystallized Microstructure

Figure 2 shows the microstructure of specimens annealed with different temperatures and times. It was found that at the same annealing temperature, the recrystallization rate of Ti steel was significantly faster than that of Ti-V steel. When annealed at 660 °C, a similar recrystallized state reached 1000 s in Ti-V steel and 300 s in Ti steel. At 690 °C, a large number of recrystallized grains were formed when the Ti steel was isothermally held for 200 s, and it was completely recrystallized when the isothermal time was 1000 s, whereas there were still more than 50% unrecrystallized grains in the Ti-V steel at 1000 s. Additionally, recrystallization was not completed until 6000 s. As shown in Figure 2f, when the annealing temperature was increased to 720 °C, more recrystallized grains were displayed with a refined grain size in the Ti-V steel after 300 s. Although the recrystallization rate of Ti-V steel was slower than that of Ti steel, its average grain size was smaller than that of Ti steel.

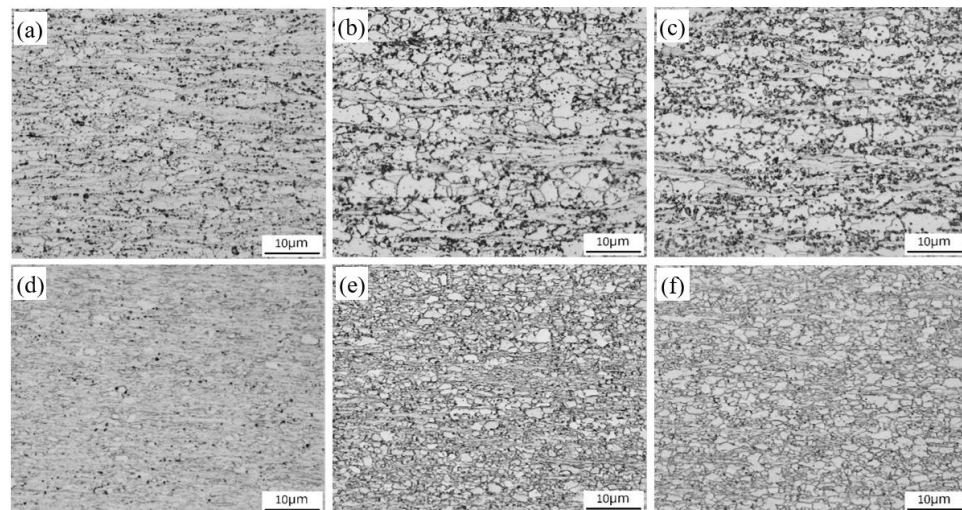


Figure 2. Microstructure of different specimens, Ti steel: (a) 660 °C, 300 s, (b) 690 °C, 200 s, (c) 720 °C, 200 s, Ti-V steel: (d) 660 °C, 1000 s, (e) 690 °C, 1000 s and (f) 720 °C, 300 s.

Figure 3 shows the misorientation map of the two steels during the recrystallization process. The blue color indicates grains that have a very small internal misorientation, which can be considered recrystallized grains, while the green, yellow and red colors represent increasing levels of internal misorientation, indicating unrecrystallized parts (for interpretation of the color coding used in this figure, the reader is referred to the web version). The fraction of recrystallized ferrite is calculated as a fraction of pixels with an average misorientation of less than 0.7° [13]. For Ti steel, after isothermal treatment for 100 s at 690 °C, the recrystallization fraction was 51.5%, which reached 86.9% after 1000 s,

whereas for Ti-V steel, the recrystallization fraction was only 7.9% after 200 s, and the recrystallization fraction was still low, 29.5%, even after 1000 s.

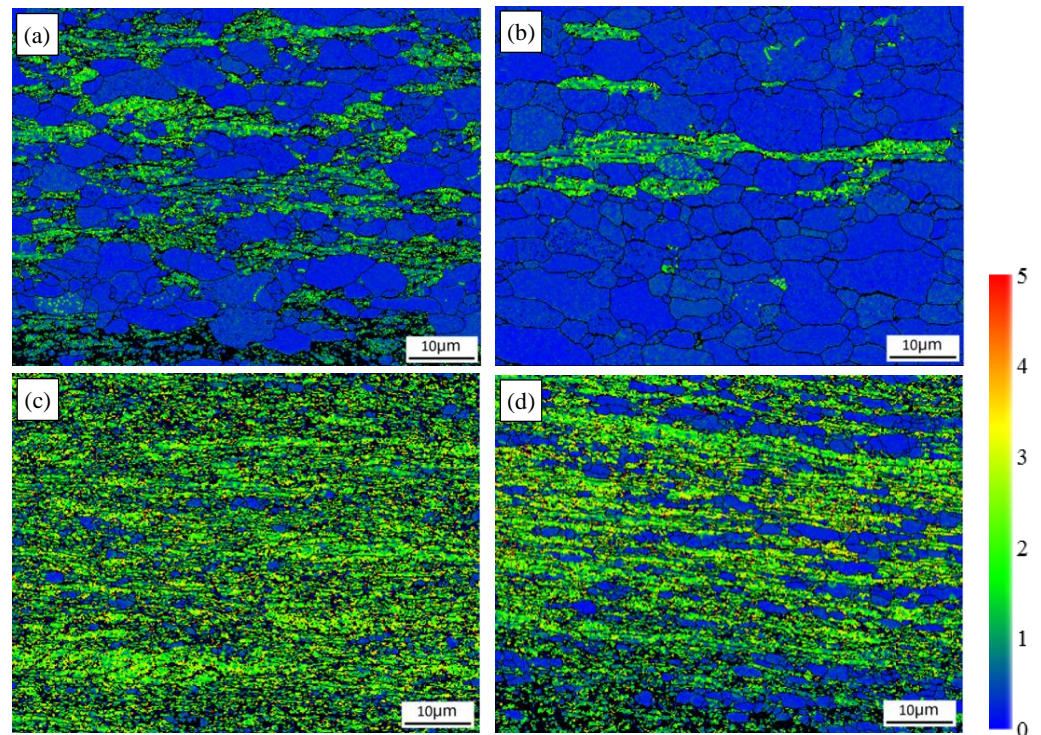


Figure 3. Misorientation map of Ti and Ti-V steel with different annealing processes at 690 °C, Ti steel: (a) 100 s, (b) 1000 s; Ti-V steel: (c) 200 s and (d) 1000 s.

3.3. Recrystallization Kinetics

In order to reduce the inhomogeneity of mechanical properties, it is necessary to obtain uniform and fine equiaxed grains through recrystallization. In this scenario, the recrystallization kinetic model is of significance in predicting the proceeding of recrystallization, which contributes to the microstructure control of cold-rolled high-strength low alloy steel in different annealing processes.

In this study, site saturation of nucleation and isotropic growth of recrystallized nuclei is assumed. The proceeding of recrystallization is affected by the deformation of stored energy and the precipitation process of the second phase [15]. The growth velocity is considered to be the product of boundary migration mobility and the driving force. It is written as follows:

$$X_{\text{ext}} = N_{\text{rex}} \cdot \frac{4\pi}{3} \left(\int_0^t M \cdot G dt \right)^3, \quad (2)$$

where X_{ext} is the extended recrystallized volume fraction, N_{rex} is the number density of recrystallized grains, M is the grain boundary mobility and G is the driving force for recrystallization. The relationship between X_{ext} and the recrystallization fraction X is shown in Equation (3):

$$X = 1 - \exp(-X_{\text{ext}}) \quad (3)$$

The driving force G is related to the stored energy which drives the boundary motion and the pinning force exerted by the particles. The stored energy is proportional to the dislocation density in the matrix, which continuously decreases as a result of the proceeding

of recrystallization. Accordingly, in this study, the stored energy was not considered to be constant but related to the recrystallized fraction. Thus, the driving force G is expressed as:

$$G = E_{\text{rex}} - \frac{3\gamma_{\text{gb}}F_V}{2R} = \frac{1}{2}\rho Gb^2(1 - X) - \frac{3\gamma_{\text{gb}}F_V}{2R} \quad (4)$$

where E_{rex} is the stored energy, which is related to the recrystallization fraction X and the initial dislocation density ρ . γ_{gb} , F_V and R represent austenite grain boundary energy, the volume fraction of precipitated phase and average precipitates radius, respectively, and μ and b are the shear modulus and the Burgers vector, respectively.

Additionally, the relationship between $\Delta\sigma_y$ and $\Delta\rho_{\text{dis}}$ and ΔH [10] is:

$$\Delta\sigma_y \approx G \cdot b \sqrt{\Delta\rho} / 2 \approx \Delta H / 3 \quad (5)$$

where $\Delta\sigma_y$, $\Delta\rho_{\text{dis}}$ and ΔH are the differences in yield strength, dislocation density and hardness between the test samples and recrystallized ones. Therefore, a quantitative relationship between initial stored energy $E_{\text{rex},0}$ and $\Delta\rho$ is built up. Ignoring the retained dislocations in complete recrystallized ferrite, $\Delta\rho$ is considered equal to the original dislocation density in the cold-rolled matrix. This means that $E_{\text{rex},0}$ is $4.8 \times 10^6 \text{ J/m}^3$ and $6.7 \times 10^6 \text{ J/m}^3$, respectively.

The grain boundary mobility M is expressed in terms of Cahn's solute drag model [6], which includes the effect of solute concentration on the mobility of the grain boundary:

$$M = \frac{M_{\text{pure}}}{1 + \sum_i \alpha_i C_i^{\text{gb}}}, \quad (6)$$

where M_{pure} refers to the intrinsic grain boundary mobility of the C-Mn steel without microalloying elements, which is estimated as 1/3 of the value of the pure matrix [16] in this study.

$$M_{\text{pure}} = \frac{D_{\text{gb}}^0}{R_{\text{gp}} T} \frac{V_{\text{Fe}}}{\lambda} \exp\left(-\frac{Q_{\text{gb}}}{R_{\text{gp}} T}\right) \quad (7)$$

where D_{gb}^0 is the pre-exponential factor, Q_{gb} is the activation energy for grain boundary mobility, V_{Fe} is ferrite molar volume ($7.11 \text{ cm}^3/\text{mol}$) and λ is the grain boundary thickness, which is assumed to be 1 nm [17]. C_i^{gb} represents the grain boundary concentration of the solute drag elements. Considering the solute segregation to the grain boundary, C_i^{gb} is given a value that is multiplied by 10 and 5 for Ti and V, respectively, to the solute concentration in the matrix [18]. α_i [19] could be obtained by:

$$\alpha_i = \frac{(RT)^2 \delta \left[\sinh\left(\frac{E_{\text{bi}}}{RT}\right) - \frac{E_{\text{bi}}}{RT} \right]}{V_{\text{m}} E_{\text{bi}} D_{\text{int}}^i} \quad (8)$$

where E_{bi} is the binding energy of the microalloying element to the grain boundary and D_{int}^i is the cross-boundary diffusion coefficient of the solute drag element. For simplicity, the grain boundary concentration in this study is assumed to be identical to that of the matrix.

The volume fraction of the precipitated particles during the recrystallization process is calculated as follows:

$$F_V = 1 - \exp\left(-\frac{4\pi}{3} N_{\text{pre}} \pi R^3\right) \quad (9)$$

where N_{pre} is the number density of precipitates nuclei formed in recrystallization.

Based on the classical nucleation theory, the nucleation rate can be expressed as:

$$I = N_0 \beta^* Z \exp\left(-\frac{\Delta G^*}{kT}\right) \exp\left(-\frac{\tau}{t}\right) \quad (10)$$

where N_0 is the number of potential nucleation sites per unit volume, β^* is the frequency factor, Z is the Zeldovich non-equilibrium factor, ΔG^* is the activation energy of nucleation, τ is incubation time, k is the Boltzmann constant, T is temperature and t is time. The parameters could be expressed as:

$$N_0 = \frac{1}{a^3} \quad (11)$$

$$\beta^* = \frac{4\pi R_c^2 D X_M}{a^4} \quad (12)$$

$$\tau = \frac{1}{2\pi\beta^*} \quad (13)$$

$$\Delta G^* = \frac{4}{3} R_c^2 \sigma \quad (14)$$

where a is the lattice parameter of ferrite, R_c is the critical nucleus radius, D is the diffusion coefficient of the microalloying elements, σ is the interfacial energy between precipitates and ferritic matrix and X_M is the concentration of microalloying elements in the matrix (For Ti steel, X_M denotes X_{Ti} and for Ti-V steel it denotes X_{Ti+V}). For common steels, both carbides and nitrides could be formed due to carbon and unavoidable nitrogen in steels. In this study, nitrogen content is limited to ~0.0012 wt% through vacuum melting and pure raw materials preparation, which means only ~0.0005 wt% Ti could be consumed by forming TiN. Thus, the influence of nitrogen is ignored, and only carbides are considered.

The critical nucleus radius of TiC:

$$R_c = \frac{2\sigma V_{TiC}}{kT} \left[\ln \frac{X_{Ti} X_C}{K_{TiC}} \right]^{-1} \quad (15)$$

The critical nucleus radius of $(Ti_x, V_{1-x})C$:

$$R_c = \frac{2\sigma V_{(Ti,V)C}}{kT} \left[\ln \frac{(X_{Ti})^x (X_V)^{1-x} X_C}{(xK_{TiC})^x [(1-x)K_{VC}]^{1-x}} \right]^{-1} \quad (16)$$

where V_{TiC} and $V_{(Ti,V)C}$ denote the molar volume of the precipitates, K_{TiC} and $K_{(Ti,V)C}$ are the solution product of TiC and $(Ti,V)C$, X_{Ti} , X_V and X_C are the solute concentrations of Ti, V and C in the matrix.

The growth rate of the precipitated particles [20] with a radius of R can be described as follows.

For TiC:

$$\frac{dR}{dt} = \frac{D}{R} \left(\frac{X_{Ti} - X_{Ti}^e}{\frac{V_m}{V_{TiC}} \cdot X_{P-Ti} - X_{Ti}^e} \right) \quad (17)$$

For $(Ti_x, V_{1-x})C$:

$$\frac{dR}{dt} = x \frac{D_{Ti}}{R} \left(\frac{X_{Ti} - X_{Ti}^e}{\frac{V_m}{V_{TiC}} \cdot X_{Ti}^p - X_{Ti}^e} \right) + (1-x) \frac{D_V}{R} \left(\frac{X_V - X_V^e}{\frac{V_m}{V_{VC}} \cdot X_{P-V} - X_V^e} \right) \quad (18)$$

where X_{Ti}^e is the equilibrium solute fraction of the microalloying element at the precipitate/matrix interface, X_p is the concentration of Ti in TiC and V_m is the molar volume of the matrix.

As stated in the literature [21], there is faster diffusion along dislocations compared to that in the matrix. In this case, the comprehensive diffusion coefficient considering the effect of dislocations is expressed as follows:

$$D = D_{dis} \pi R_{core}^2 \rho + D_{bulk} \left(1 - \pi R_{core}^2 \rho \right) \quad (19)$$

where D_{dis} is the diffusion coefficient for the pipe diffusion along dislocations, D_{bulk} is the bulk diffusion coefficient and R_{core} is the radius of the dislocation core. ρ is the dislocation density which is considered as:

$$\rho = (1 - X)\rho_0 \quad (20)$$

where ρ_0 is the original dislocation density, which can be obtained using Equation (5).

D_{dis} is written as:

$$D_{\text{dis}} = m_{\text{dis}}D_{\text{bulk}} \quad (21)$$

where D_{bulk} is expressed as $D_{0-\text{Ti}} \exp(-Q_{\text{act-Ti}}/RT)$ and $D_{0-\text{V}} \exp(-Q_{\text{act-V}}/RT)$ for Ti and V, respectively. m_{dis} is a correction factor, which can be defined according to:

$$m_{\text{dis}} = 0.0133 \exp(11,500/RT) \quad (22)$$

The values of parameters used in the recrystallization model are shown in Table 2. The values were determined according to the literature or adjusted to fit the range of experimental data.

Table 2. Values of the key parameters used in the recrystallization model.

Symbol	Description	Unit	Value	Ref.
N_{rex}	Number Density of Recrystallization Nucleation Sites of Ti steel	m^{-3}	8×10^{14}	5.0×10^{14} [22] 2×10^{15} [11]
	Number Density of Recrystallization Nucleation Sites of Ti-V steel	m^{-3}	9×10^{14}	5.0×10^{14} [22] 2×10^{15} [11]
$E_{\text{rex},0}$	Stored energy of Ti steel	J/m^3	4.8×10^6	This work
	Stored energy of Ti-V steel	J/m^3	6.5×10^6	This work
γ_{gb}	Grain Boundary Energy	J/m^2	0.72	0.75 [17]
D_{gb}^0	Prefactor for Grain Boundary Mobility	m^2/s	6.9×10^{-5}	1.5×10^{-4} [22]
Q_{gb}	Activation Energy for Grain Boundary Mobility	J/mol	3.25×10^5	1.48×10^5 [22] 2.53×10^5 [17]
	Ti-binding energy with grain boundary	J/mol	1.4×10^4	[23]
E_{b}	V-binding energy with grain boundary	J/mol	1.0×10^4	[23]
	Bulk diffusion coefficient of Ti	m^2/s	1.4×10^{-5}	[24]
D_0	Bulk diffusion coefficient of V	m^2/s	2.4×10^{-5}	[25]
	Activation energy of Ti	kJ/mol	240	[24]
Q_{act}	Activation energy of V	kJ/mol	260	[25]
δ	Grain boundary thickness	nm	0.25	
V_{m}	Molar volume of α iron	m^3/mol	7.11×10^{-6}	
V_{p}	Molar volume of TiC	m^3/mol	1.21×10^{-5}	
	Molar volume of VC	m^3/mol	1.1×10^{-5}	

Figure 4 shows the evolution of the radius and number density of the precipitates during the isothermal treatment at different temperatures. Generally, the radius increases while the number density increases first and reaches a plateau with the increase in annealing time. One can also see that the radius of TiC is larger than $(\text{Ti}_x\text{V}_{1-x})\text{C}$, and the number density of the latter is higher. Moreover, the radius increases, whereas the number density decrease with the increase in the annealing temperature.

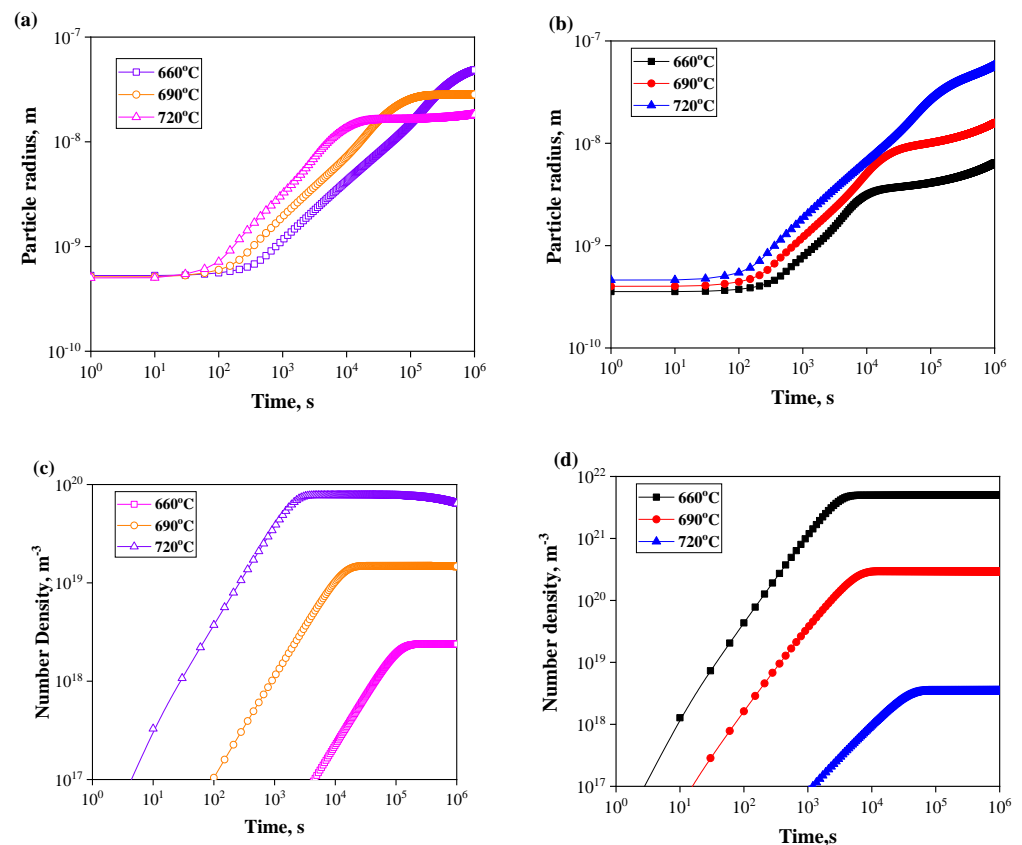


Figure 4. Radius and number density of precipitates during isothermal treatment at different temperatures: (a) radius of TiC, (b) radius of $(\text{Ti}_x, \text{V}_{1-x})\text{C}$, (c) number density of TiC and (d) number density of $(\text{Ti}_x, \text{V}_{1-x})\text{C}$.

As shown in Figure 5a, the driving force maintains a high value at the beginning, which is due to the lower recrystallization fraction as well as the lower precipitates fraction. With the proceeding of recrystallization and precipitation, the driving force decreases drastically. Compared to Ti steel, the driving force of Ti-V steel remains higher for the same isothermal treatment, whereas in Figure 5b, one can see that the grain boundary mobility of Ti-V steel is much lower than that of Ti steel. This results from the fact that higher solute concentration in Ti-V steel provides enough solute drag to the grain boundaries. Moreover, it was found that there is a decrease in the value of D_{int}^i with the decrease in dislocation density with the proceeding of recrystallization (as shown in Figure 6). In this scenario, the grain boundary mobility is decreased due to the increase in α_i , while with prolonged isothermal time, the solute concentration decreases so that the solute drag effect is weakened, responsible for the increase in mobility.

Figure 7 represents the modeled fraction of recrystallized ferrite, and experimental data are added. There is a good agreement between the model and experiments for both steels investigated, even though there are some larger deviations with some data. The sources of the error may come from the actual influence of N or the choice of the fitting parameters. However, in general, the model is able to reproduce the effect of microalloying elements on recrystallization, i.e., the higher concentration of microalloying elements could more effectively retard the proceeding of recrystallization. When the annealing temperature of the Ti steel is 660 °C, it takes approximately 520 s to reach the recrystallization fraction of 50%, and the recrystallization fraction is 70% when the isothermal temperature is about 1000 s. When the annealing temperature rises to 690 °C, the recrystallization process is almost completed at 1000 s. When the annealing temperature is 720 °C, the recrystallization completion time is significantly shortened, and more than 90% recrystallization is achieved

at an isothermal time of 500 s. Comparing the recrystallization volume fraction curves at different temperatures, the recrystallization process of Ti-V steel is obviously slower than that of Ti steel. Additionally, it was found that the recrystallization fraction measured by EBSD is consistent with the calculation result of the softening rate formula.

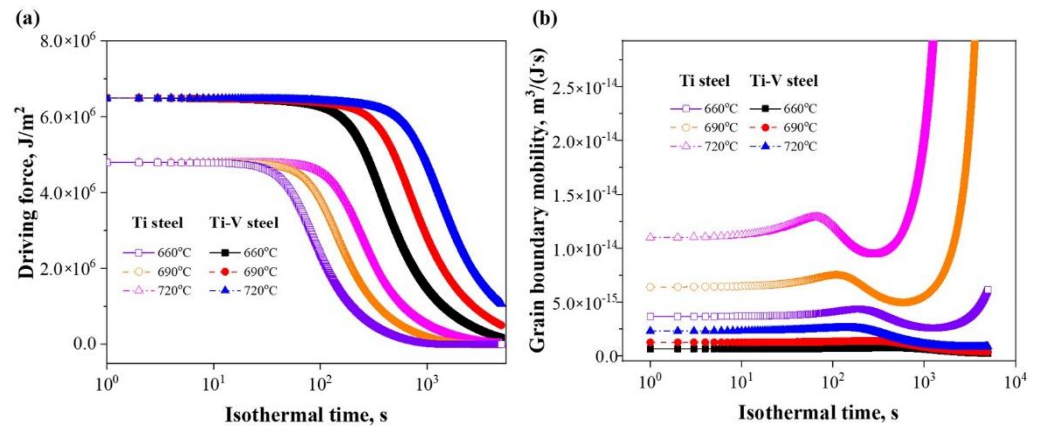


Figure 5. Driving force and grain boundary mobility versus isothermal time for varied temperature: (a) driving force and (b) grain boundary mobility.

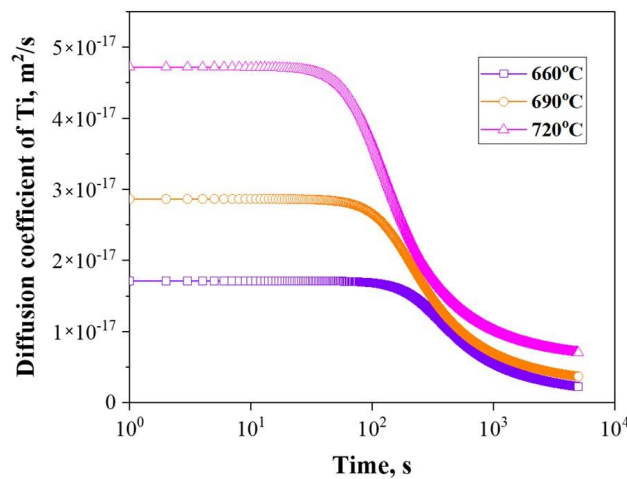


Figure 6. Variation of diffusion coefficient of Ti during isothermal treatment at different temperatures of Ti steel.

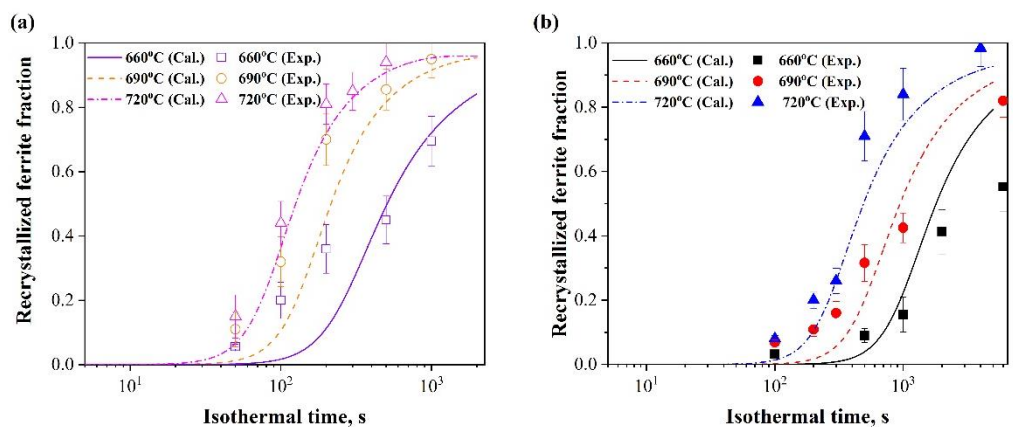


Figure 7. Comparison between calculated and measured recrystallized fraction of different steels at a series of different temperatures (660, 690, 720 °C): (a) Ti steel and (b) Ti-V steel.

Additionally, the recrystallized grain size is calculated in this model, as shown in Figure 8, which is in good agreement with that of the metallography measurement.

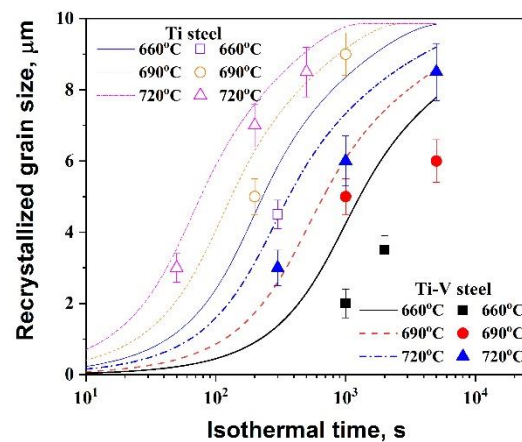


Figure 8. Comparison between calculated and measured recrystallized grain size of Ti and Ti-V steels at a series of different temperatures (660, 690, 720 °C).

During the annealing of the cold-rolled sheet, the precipitation and recrystallization process proceeds simultaneously. From Expressions (4) and (5), it can be seen that the recrystallization process is significantly affected by the precipitation behavior, especially the volume fraction of precipitates, the average precipitates radius and the solute concentration of microalloying element, i.e., the higher the volume fraction of the precipitates, the smaller the size of the precipitated particles, and the larger the concentration of solute microalloying elements, the more hindered recrystallization it will have.

On the other hand, the change of the dislocation density during the recrystallization process will affect the nucleation position of the precipitated particles, thereby affecting the precipitation behavior, but this is not considered in the model. Moreover, the solid solution atoms will have a drag effect on the grain boundary movement during the recrystallization process [12], and the precipitation behavior will affect the content of solid solution atoms, which will have a certain impact on the recrystallization. Given the fact that recrystallization proceeds more sluggish in Ti-V steel, it is indicated that the solute drag is more effective in retarding the recrystallization, which is in accordance with Hutchinson's research [9].

4. Conclusions

In this study, the recrystallization kinetics of two HSLA steels with microalloying elements of Ti and Ti+V were investigated. The main conclusions from this work are as follows.

- (1) The recrystallization kinetics of the Ti+V steel are slowed down compared to the Ti steel.
- (2) Based on solid solution theory, mass conservation law and classical nucleation, growth and coarsening theory, the precipitation behavior of Ti and Ti+V steels was predicted. The radius of TiC was larger than $(Ti_x, V_{1-x})C$, and the number density of the latter was higher.
- (3) By considering the effect of recrystallization on stored energy and the influence of the microalloyed precipitates and microalloying solutes on the driving force and grain boundary mobility, the model of the recrystallization kinetics was proposed. The proposed recrystallization model can describe the recrystallization kinetics and grain size evolution well. Solute drag is more effective in retarding recrystallization than the pinning effect of precipitates.

Author Contributions: Conceptualization, S.T.; data curation, S.T.; formal analysis, S.T.; methodology, S.T.; experiment, S.T.; formal analysis, S.T.; investigation, S.T. and X.L.; visualization, X.L.; writing—original draft preparation, S.T.; writing—review and editing, S.T.; supervision, J.L. and Z.L.; project administration, G.W. All authors have read and agreed to the published version of the manuscript.

Funding: This study was supported by the National Natural Science Foundation of China (Grant Nos. 52175293, 51774083 and 51774082), the Fundamental Research Funds for the Central Universities (Grant Nos. N2007002 and N2007011) and the 111 Project (Grant No. B20029).

Institutional Review Board Statement: Not applicable.

Informed Consent Statement: Not applicable.

Data Availability Statement: The data required to reproduce these findings cannot be shared at this time.

Conflicts of Interest: The authors declare no conflict of interest.

References

1. Kashima, T.; Hashimoto, S.; Mukai, Y. 780 N/mm² grade hot-rolled high-strength steel sheet for automotive suspension system. *JSAE Rev.* **2003**, *24*, 81–86. [[CrossRef](#)]
2. Takahashi, M. Development of High Strength Steels for Automobiles. *Nippon Steel Tech. Rep.* **2003**, *88*, 2–7.
3. Zhang, X.; Loannidou, C.; Ten Brink, G.H.; Navarro-López, A.; Wormann, J.; Campaniello, J.; Dalglish, R.M.; van Well, A.A.; Offerman, S.E.; Kranendonk, W.; et al. Microstructure, precipitate and property evolution in cold-rolled Ti-V high strength low alloy steel. *Mater. Des.* **2020**, *192*, 108720. [[CrossRef](#)]
4. Chen, C.; Liao, M. Synergistic effects of carbon content and Ti/Mo ratio on precipitation behavior of HSLA steel: Insights from experiment and critical patent analysis. *Mater. Des.* **2020**, *186*, 108361. [[CrossRef](#)]
5. Ooi, S.W.; Fourlaris, G. A comparative study of precipitation effects in Ti only and Ti-V Ultra Low Carbon (ULC) strip steels. *Mater. Charact.* **2006**, *56*, 214–226. [[CrossRef](#)]
6. Cahn, J.W. The impurity-drag effect in grain boundary motion. *Acta Metall.* **1962**, *10*, 789–798. [[CrossRef](#)]
7. Hillert, M.; Sundman, B. A treatment of the solute drag on moving grain boundaries and phase interfaces in binary alloys. *Acta Metall.* **1976**, *24*, 731–743. [[CrossRef](#)]
8. Hersent, E.; Marthinsen, K.; Nes, E. On the Effect of Atoms in Solid Solution on Grain Growth Kinetics. *Metall. Mater. Trans. A* **2014**, *45*, 4882–4890. [[CrossRef](#)]
9. Hutchinson, C.R.; Zurob, H.S.; Sinclair, C.W.; Brechet, Y.J.M. The comparative effectiveness of Nb solute and NbC precipitates at impeding grain-boundary motion in Nb steels. *Scr. Mater.* **2008**, *59*, 635–637. [[CrossRef](#)]
10. Kulakov, M.; Poole, W.J.; Militzer, M. The Effect of the Initial Microstructure on Recrystallization and Austenite Formation in a DP600 Steel. *Metall. Mater. Trans. A* **2013**, *44*, 3564–3576. [[CrossRef](#)]
11. Bellavoine, M.; Dumont, M.; Drillet, J.; Hébert, V.; Maugis, P. Combined Effect of Heating Rate and Microalloying Elements on Recrystallization during Annealing of Dual-Phase Steels. *Metall. Mater. Trans. A* **2018**, *49*, 2865–2875. [[CrossRef](#)]
12. Philippot, C.; Bellavoine, M.; Dumont, M.; Hoummada, K.; Drillet, J.; Hébert, V.; Maugis, P. Influence of Heating Rate on Ferrite Recrystallization and Austenite Formation in Cold-Rolled Microalloyed Dual-Phase Steels. *Metall. Mater. Trans. A* **2017**, *49*, 66–77. [[CrossRef](#)]
13. Castro Cerda, F.M.; Vercruyssen, F.; Minh, T.N.; Kestens, L.; Monsalve, A.; Petrov, R. The Effect of Heating Rate on the Recrystallization Behavior in Cold Rolled Ultra Low Carbon Steel. *Steel Res. Int.* **2017**, *88*, 1600351. [[CrossRef](#)]
14. Liu, Z.; Olivares, R.O.; Lei, Y.; Garcia, C.I.; Wang, G. Microstructural characterization and recrystallization kinetics modeling of annealing cold-rolled vanadium microalloyed HSLA steels. *J. Alloys Compd.* **2016**, *679*, 293–301. [[CrossRef](#)]
15. Zurob, H.S.; Brechet, Y.; Purdy, G. A model for the competition of precipitation and recrystallization in deformed austenite. *Acta Mater.* **2001**, *49*, 4183–4190. [[CrossRef](#)]
16. Zhou, T.; O'malley, R.J.; Zurob, H.S. Study of Grain-Growth Kinetics in Delta-Ferrite and Austenite with Application to Thin-Slab Cast Direct-Rolling Microalloyed Steels. *Metall. Mater. Trans. A* **2010**, *41*, 2112–2120. [[CrossRef](#)]
17. Zurob, H.S.; Hutchinson, C.R.; Brechet, Y.; Purdy, G. Modeling recrystallization of microalloyed austenite: Effect of coupling recovery, precipitation and recrystallization. *Acta Mater.* **2002**, *50*, 3077–3094. [[CrossRef](#)]
18. Buken, H.; Kozeschnik, E. A Model for Static Recrystallization with Simultaneous Precipitation and Solute Drag. *Metall. Mater. Trans. A* **2016**, *48*, 2812–2818. [[CrossRef](#)]
19. Jin, H.; Elfimov, I.; Militzer, M. Study of the interaction of solutes with $\Sigma 5$ (013) tilt grain boundaries in iron using density-functional theory. *J. Appl. Phys.* **2014**, *115*, 93506. [[CrossRef](#)]
20. Perez, M.; Dumont, M.; Acevedo-Reyes, D. Implementation of classical nucleation and growth theories for precipitation. *Acta Mater.* **2008**, *56*, 2119–2132. [[CrossRef](#)]
21. Dutta, B.; Palmiere, E.J.; Sellars, C.M. Modelling the kinetics of strain induced precipitation in Nb microalloyed steels. *Acta Mater.* **2001**, *49*, 785–794. [[CrossRef](#)]

22. Sinclair, C.W.; Hutchinson, C.R.; Bréchet, Y. The Effect of Nb on the Recrystallization and Grain Growth of Ultra-High-Purity α -Fe: A Combinatorial Approach. *Metall. Mater. Trans. A* **2007**, *38*, 821–830. [[CrossRef](#)]
23. Jin, H.; Elfimov, I.; Militzer, M. First-principles simulations of binding energies of alloying elements to the ferrite-austenite interface in iron. *J. Appl. Phys.* **2018**, *123*, 85303. [[CrossRef](#)]
24. Marceaux Dit Clément, A.; Hoummada, K.; Drillet, J.; Hébert, V.; Maugis, P. Delaying Effect of Cementite on Recrystallization Kinetics of a Ti-Nb Microalloyed High-Formability Steel. *Metall. Mater. Trans. A Phys. Metall. Mater. Sci.* **2020**, *51*, 4059–4073. [[CrossRef](#)]
25. Marynowski, P.; Adrian, H.; Głowacki, M. Modeling of the Kinetics of Carbonitride Precipitation Process in High-Strength Low-Alloy Steels Using Cellular Automata Method. *J. Mater. Eng. Perform.* **2019**, *28*, 4018–4025. [[CrossRef](#)]